MDPI

Article

Nickel Foam-Supported Hierarchical NiCo$_2$S$_4$ Nanostructures as Efficient Electrocatalysts for the Methanol Oxidation Reaction

Dan Jin [1], Wenting Cheng [2], Shaoyun Wu [3], Zhen Li [4,*] and Zhenghua Wang [2,*]

[1] School of Pharmacy, Wannan Medical College, Wuhu 241002, China; jindan@wnmc.edu.cn
[2] Key Laboratory of Functional Molecular Solids, Ministry of Education, College of Chemistry and Materials Science, Anhui Normal University, Wuhu 241000, China; 2121011263@ahnu.edu.cn
[3] Wuhu Medical and Health School, Wuhu 241100, China; ahxgx@163.com
[4] College of Food Engineering, Anhui Science and Technology University, Fengyang 233100, China
[*] Correspondence: lizhen@ahstu.edu.cn (Z.L.); zhwang@ahnu.edu.cn (Z.W.)

Abstract: In this study, hierarchical NiCo$_2$S$_4$ nanostructures have been successfully prepared on Ni foam support using a simple and economical two-step hydrothermal process. The hierarchical NiCo$_2$S$_4$ nanostructure comprises rod-like NiCo$_2$S$_4$ cores enveloped by a thin nanoribbon shell. When the NiCo$_2$S$_4$/Ni foam was employed as an electrode for methanol electrooxidation directly, a current density of 194 mA mg^{-1} was achieved at 0.60 V. The prepared NiCo$_2$S$_4$/Ni foam demonstrates high electrocatalytic activity and durability in alkaline environments for the methanol oxidation reaction. After 1000 cyclic voltammetry cycles in the alkaline electrolyte, the current density of the hierarchical NiCo$_2$S$_4$ decreased to 72.2% of its initial value, with the loss of catalytic activity during the cycling test attributed to their surface oxidation. These findings suggest the NiCo$_2$S$_4$ sample as a non-noble metal electrocatalyst holds great potential for direct methanol fuel cells.

Keywords: NiCo$_2$S$_4$; methanol oxidation reaction; hierarchical nanomaterial; electrocatalyst

check for updates

1. Introduction

Due to social progress and excessive consumption of non-renewable resources, the demand for human energy is rising, resulting in the use of traditional fossil fuels such as coal, oil, and natural gas, which is also increasing rapidly. First of all, the traditional non-renewable fossil energy reserves are limited, and the rapid increase in energy consumption makes fossil energy gradually depleted. Secondly, the carbon dioxide released during the use of fossil energy produces many serious environmental pollution problems such as climate warming, dust, acid rain, haze, and so on. As a result, people in the 21st century are facing serious challenges such as environmental pollution and the energy crisis. Addressing the twin challenges requires a concerted push towards reforming our energy structure. This includes the development of renewable, efficient, and low-carbon energy alternatives to traditional fossil fuels. As the importance of green and clean energy escalates, Direct Methanol Fuel Cells (DMFCs) have been gaining increased attention as a promising research focus. DMFCs use methanol as fuel, and the method of obtaining methanol is very extensive and cheap. Secondly, in the practical application process of fuel cells, methanol is convenient for transportation and safe storage. In addition, the main product of DMFCs is water, which is also in line with the important direction of sustainable development of green energy and environmental protection pursued in the 21st century. Thus, as a novel, efficient, and clean electrochemical energy conversion device, DMFCs offer broad prospects in the field of new energy research [1–8].

DMFCs predominantly consist of two half-reactions: anodic oxidation and cathodic reduction. The anodic Methanol Oxidation Reaction (MOR) involves the oxidation of CH$_3$OH to CO$_2$, a process characterized by a six-electron transfer reaction. The kinetic rate of this electrode reaction is slow, and the performance of the catalyst is a key factor

influencing this rate. At present, platinum-based noble metal catalysts are the most effective and stable catalysts in the catalytic oxidation process of methanol. Noble metal catalysts exhibit high catalytic activity for MOR in DMFCs [9–13], but their drawbacks—Such as high cost, limited reserves, and susceptibility to CO poisoning—Hinder their large-scale commercial production and application. Compared with noble metal catalysts, non-precious metals show great cost advantages. People try to greatly improve the catalytic performance of such materials so as to achieve the purpose of replacing noble metal catalysts. Thus, the exploration and development of low-cost, abundant, highly active, and stable non-noble metal anode electrocatalysts are of paramount importance.

Transition metal sulfides, with their abundant reserves, low cost, diverse compositional structures, excellent conductivity, and mechanical properties, hold vast application potential in optics, energy storage, catalysis, and other aspects [14–17]. Sulfur atoms, having a larger atomic radius and lower electronegativity than oxygen atoms, facilitate greater orbital overlap during bonding in binary metal sulfide, resulting in higher electrical conductivity than oxides and a stronger synergistic effect between metal ions. Consequently, transition metal sulfides exhibit superior electrical conductivity and electrochemical activity compared to oxides. Despite the limited research on $NiCo_2S_4$ nanomaterials as electrocatalysts for MOR [18,19], various Ni-Co binary metal sulfides have demonstrated excellent performance in energy storage, as supercapacitor active materials, and as MOR electrocatalysts [20–23]. However, there are still some problems with the application of transition metal sulfides, such as the low conductivity and the use of binders in the preparation of electrodes, which reduce the electrochemical performance. Ni foam with a 3D porous structure is considered the most suitable base material because of its good mechanical properties, high electrical conductivity, and good stability. The active material grown in situ on Ni foam can be used directly as an electrode without any binder and in tight contact. Therefore, the above problems can be effectively improved by growing the active materials directly on the conductive substrate of Ni foam.

Therefore, hierarchical $NiCo_2S_4$ nanostructures supported on Ni foam were successfully prepared via a simple and economical hydrothermal synthesis and anion exchange process in this study. The hierarchical $NiCo_2S_4$ nanostructure is comprised of a $NiCo_2S_4$ nanorod core enwrapped by a thin nanoribbon shell. The $NiCo_2S_4$ nanomaterial had a novel hierarchical structure and not only had a large specific surface area but could also fully contact the electrolyte, showing good electrocatalytic performance. $NiCo_2S_4$ had been used as an electrocatalyst for MOR, allowing for optimal contact between the active material and the electrolyte. In an alkaline electrolyte, the prepared hierarchical $NiCo_2S_4$ nanostructure demonstrated excellent electrocatalytic properties and durability for methanol oxidation. These findings show the prepared $NiCo_2S_4$ sample is a promising non-noble metal electrocatalyst for DMFCs.

2. Results and Discussion

2.1. Phase and Microscopic Morphology Analysis

To preclude any influence from the Ni foam, the samples were detached prior to characterization. The composition of the products was analyzed using X-ray Diffraction (XRD). The main diffraction peaks of the precursor, as displayed in Figure S1, separately correspond to $Co(CO_3)_{0.5}(OH) \cdot 0.11H_2O$ and $Ni_{6.1}Co_{2.9}(OH)_{18.27}(CO_3)_{1.315} \cdot 6.7H_2O$. These results indicate that the precursor is mainly composed of a carbonate hydroxide phase. Figure 1 also presents a typical XRD pattern for the final sample. The primarily diffraction peaks at 2θ values of 16.3°, 26.7°, 31.3°, 38.2°, 50.3°, and 55.2° separately align with the (111), (220), (311), (400), (511), and (440) planes of the cubic phase $NiCo_2S_4$ (JCPDS No. 43-1477). The absence of any extraneous peaks in the synthesized samples testifies to their purity. These findings confirm that the primary constituent of the obtained sample is $NiCo_2S_4$.
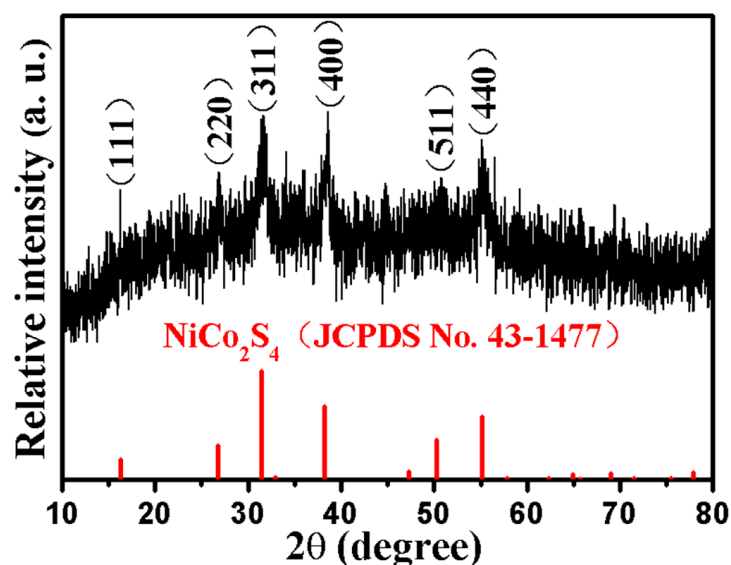
Figure 1. XRD pattern of the $NiCo_2S_4$ sample.

To gain a more comprehensive understanding of the surface morphology of the prepared products, Scanning Electron Microscopy (SEM) and Transmission Electron Microscopy (TEM) were employed for characterization. Figure 2a,b depict the images of the precursor, which appear to be composed of uniform nanorods. The nanorods of the precursor exhibit a needle-like form and are solid in nature. SEM images of the $NiCo_2S_4$ product are presented at different magnifications in Figure 3, which can provide further insights. The low-magnification SEM image (Figure 3a) illustrates the even dispersion of the $NiCo_2S_4$ sample on the Ni foam. Magnified SEM images shown in Figure 3b,c uncover the presence of a multitude of rod-like nanomaterials within the $NiCo_2S_4$ sample. Figure 3d offers a high-magnification view of $NiCo_2S_4$. As shown in the figure, the red arrow represents $NiCo_2S_4$ with a rod-like structure, and the blue arrow is nanoribbon shells wrapped around it. It can be seen that the rod-like $NiCo_2S_4$ is enwrapped by a thin nanoribbon shell. Consequently, the SEM images illustrate that $NiCo_2S_4$ exhibits a typically hierarchical nanostructure. This type of hierarchical structure, with its large surface area, is conducive to electrocatalytic reactions.
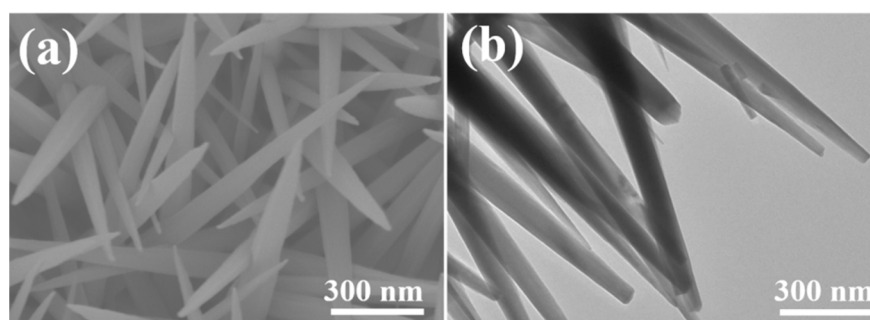

Figure 2. (**a**) SEM; (**b**) SEM images of the precursor.

The morphology of the as-synthesized $NiCo_2S_4$ sample is further elucidated by TEM, as displayed in Figure 4a. The image reveals a nanorod core enveloped by extremely thin nanoribbons, resulting in hierarchical nanostructures through the vulcanization process. A High-Resolution TEM (HRTEM) image for the $NiCo_2S_4$ sample is presented in Figure 4b. In this image, the lattice fringes display adjacent distances of 0.181 nm and 0.236 nm, separately corresponding to the (511) and (400) crystal planes of the spinel $NiCo_2S_4$.
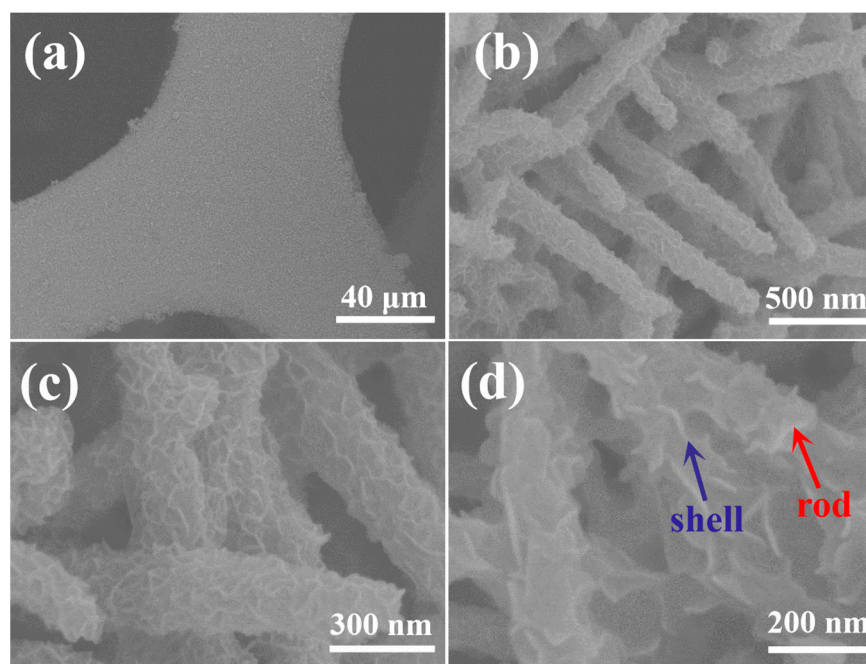
Figure 3. SEM images of the $NiCo_2S_4$ sample at different magnifications: (**a**) 40 μm; (**b**) 500 nm; (**c**) 300 nm; (**d**) 200 nm.
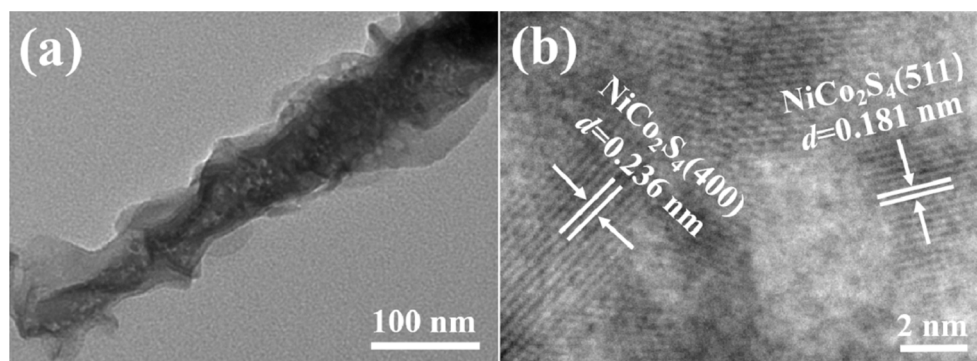
Figure 4. (**a**) TEM; (**b**) HRTEM images of the $NiCo_2S_4$ sample.

2.2. XPS Analysis

X-ray Photoelectron Spectroscopy (XPS) had been employed to confirm the surface elemental composition and the chemical state of the $NiCo_2S_4$ sample. The XPS peaks had been fitted according to the Gauss-Lorentz equation. A broad-range XPS spectrum in the range of 0–1100 eV, presented in Figure 5a, verifies the presence of Ni 2p, Co 2p, and S 2p elements in the $NiCo_2S_4$ sample, with the appearance of O and C elements (used as a reference) attributed to the adsorption of carbon dioxide on the sample surface [24]. Figure 5b illustrates a Ni 2p XPS spectrum, containing spin-orbit doublets at 856.5 eV (Ni $2p_{3/2}$) and 874.4 eV (Ni $2p_{1/2}$), which accompany their respective satellite peaks (marked as "Sat.") at 861.7 and 881.3 eV [25]. These spin-orbit doublets correspond to the Ni^{2+} and Ni^{3+} oxidation states, showing the presence of both Ni^{2+} and Ni^{3+} in the $NiCo_2S_4$ sample [26,27]. In Figure 5c, a Co 2p spectrum features spin-orbit doublets at 781.9 eV (Co $2p_{3/2}$) and 797.9 eV (Co $2p_{1/2}$), along with satellite peaks (marked as "Sat.") at 786.3 and 803.1 eV, signifying the Co^{3+} and Co^{2+} oxidation states present in the product [28,29]. Finally, Figure 5d displays the binding energies of the S 2p spectrum at 161.5 and 162.9 eV, corresponding to S $2p_{3/2}$ and S $2p_{1/2}$. In addition, there is a peak at 168.9 eV aligning well with the signature of surface sulfur oxides [30] and another peak at 170.1 eV attributed to

the satellite peaks. The results of the XPS spectra confirm that the Ni, Co, and S elements in $NiCo_2S_4$ have abundant oxidation states.

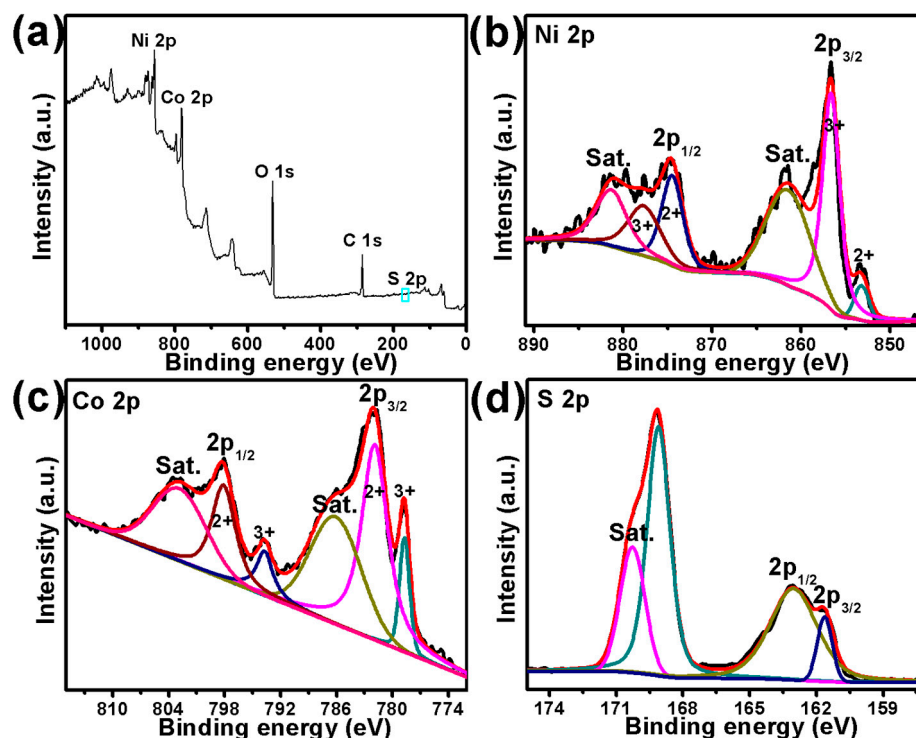**Figure 5.** XPS spectra of the $NiCo_2S_4$ sample: (**a**) survey scan; (**b**) Ni 2p; (**c**) Co 2p; (**d**) S 2p.

2.3. Specific Surface Area

The specific surface area and pore size distribution of $NiCo_2S_4$ nanostructures are depicted in Figure 6. As displayed in Figure 6a, the N_2 adsorption-desorption isotherms for the $NiCo_2S_4$ product present type IV isotherms with obvious H3 hysteresis loops, a characteristic typically found in sheet-like nanomaterials, aligning with the SEM and TEM images for $NiCo_2S_4$. The pore size distribution curve, illustrated in Figure 6b, reveals that the pore size of $NiCo_2S_4$ predominantly falls between 2 and 15 nm, indicating the traits of mesoporous materials. Furthermore, according to the Brunauer-Emmett-Teller (BET) method, the surface area of the $NiCo_2S_4$ sample was 23.2 m^2 g^{-1}, which could provide an abundance of active sites for catalyzing methanol reactions.

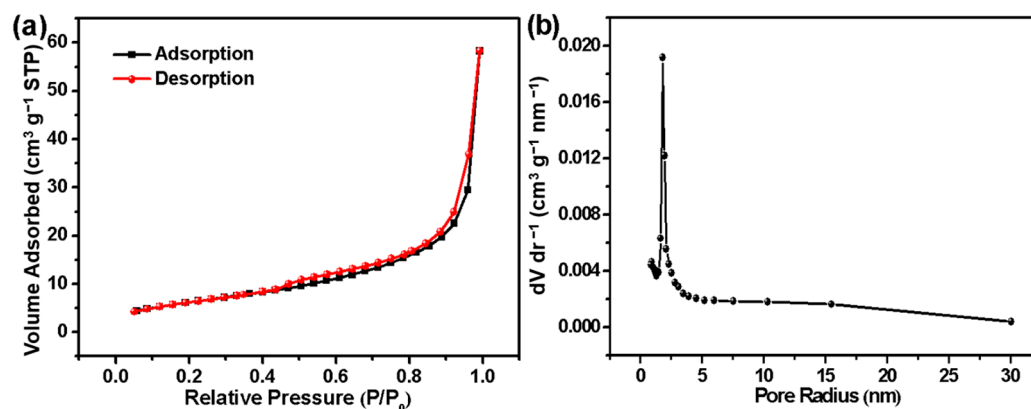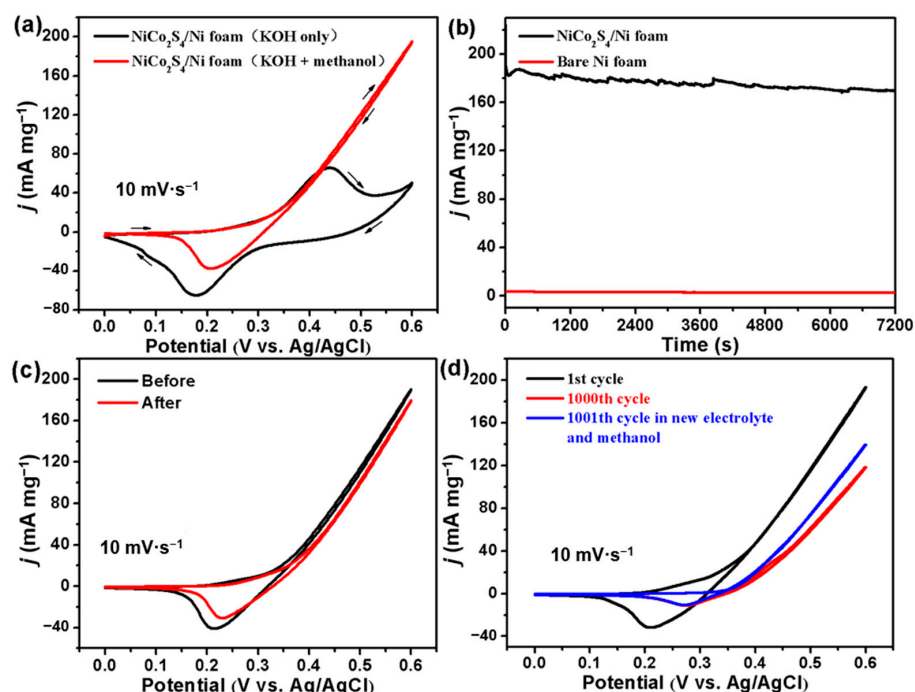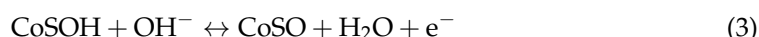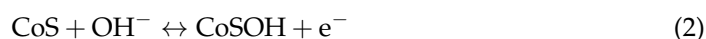**Figure 6.** (**a**) N_2 adsorption-desorption isotherms; (**b**) BJH pore size distribution curve of the $NiCo_2S_4$ sample.
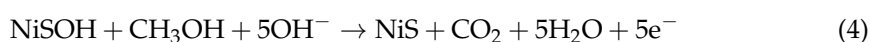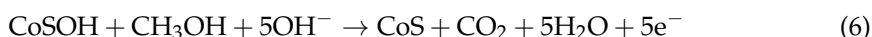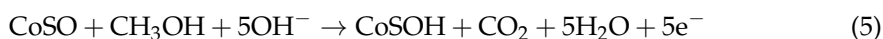
2.4. Electrocatalytic Performances for MOR

The performance of the active materials has been evaluated using cyclic voltammetry (CV) and chronoamperometry (CA) on a three-electrode system. As displayed in Figure 7a, the typical CV curves of the $NiCo_2S_4$/Ni foam electrode had been executed in a 1 mol dm^{-3} KOH electrolyte solution between 0 and 0.60 V (vs. Ag/AgCl). It can be seen that the CV curve presents a pair of redox peaks in the electrolyte without methanol, indicative of reversible Faradaic redox reactions occurring on the surface of $NiCo_2S_4$ in an alkaline electrolyte. Their probable reactions are given as follows [31,32]:

$$NiS + OH^- \leftrightarrow NiSOH + e^- \tag{1}$$

$$CoS + OH^- \leftrightarrow CoSOH + e^- \tag{2}$$

$$CoSOH + OH^- \leftrightarrow CoSO + H_2O + e^- \tag{3}$$

Figure 7. (**a**) CV curves of the $NiCo_2S_4$/Ni foam electrode in 1 mol dm^{-3} KOH electrolyte with and without 0.5 mol dm^{-3} methanol; (**b**) Chronoamperograms of the $NiCo_2S_4$/Ni foam and bare Ni foam electrodes at 0.60 V (vs. Ag/AgCl) with a duration of 7200 s; (**c**) CV curves of the $NiCo_2S_4$/Ni foam electrode in 1 mol dm^{-3} KOH and 0.5 mol dm^{-3} methanol before and after chronoamperometry test for 7200 s; (**d**) CV curves of the $NiCo_2S_4$/Ni foam electrode in 1 mol dm^{-3} KOH and 0.5 mol dm^{-3} methanol at the first and the 1000th cycle and the CV curve at the 1001th cycle in new KOH electrolyte and methanol.

The CV curve displays a different profile in a 1 mol dm^{-3} KOH alkaline electrolyte with 0.5 mol dm^{-3} methanol. In the forward scan, the curve aligns closely with the one obtained without methanol in the potential range of 0–0.41 V. Beyond the potential of 0.41 V, a sharp increase in current density is observed, which is attributable to methanol electrooxidation on the $NiCo_2S_4$. As depicted in Figure 7a, the current density at 0.60 V of the $NiCo_2S_4$ sample is 194 mA mg^{-1}, suggesting that this sample demonstrates superior electrocatalytic activity for the methanol oxidation reaction. The half reactions of the methanol oxidation on $NiCo_2S_4$ are given below:

$$NiSOH + CH_3OH + 5OH^- \rightarrow NiS + CO_2 + 5H_2O + 5e^- \tag{4}$$

$$CoSO + CH_3OH + 5OH^- \rightarrow CoSOH + CO_2 + 5H_2O + 5e^- \tag{5}$$

$$CoSOH + CH_3OH + 5OH^- \rightarrow CoS + CO_2 + 5H_2O + 5e^- \tag{6}$$

In order to investigate the role of each metal element in the electrocatalytic reaction, NiS and Co_9S_8 were synthesized on Ni foam by the same two-step hydrothermal method above, and their electrocatalytic activity for MOR was tested. The CV curves of NiS/Ni foam, Co_9S_8/Ni foam, and $NiCo_2S_4$/Ni foam electrodes in 1 mol dm^{-3} KOH electrolyte with 0.5 mol dm^{-3} methanol and without methanol are shown and compared in Figure S2. The CV curves of these three electrodes in a 1 mol dm^{-3} KOH electrolyte without 0.5 mol dm^{-3} methanol showed similar characteristics, all showing Faraday redox peaks. $NiCo_2S_4$/Ni foam has a larger integrated area of the CV curve, indicating that its electrochemical activity is higher than NiS/Ni foam and Co_9S_8/Ni foam electrodes. When 0.5 mol dm^{-3} methanol was added to 1 mol dm^{-3} KOH electrolyte, the current density of the CV curve increased sharply from about 0.25 V at positive sweep. At a potential of 0.6 V, the current densities of the NiS/Ni foam, Co_9S_8/Ni foam, and $NiCo_2S_4$/Ni foam electrodes are 106, 129, and 194 mA mg^{-1}, respectively. It can be seen that the catalytic activity of these sulfides is in the following order: $NiCo_2S_4$ > Co_9S_8 > NiS. As a result, the Ni-Co binary metal sulfide displays better electrocatalytic activity than the relevant mono-metallic sulfide, which is mainly due to the synergistic effect between Co and Ni ions.

Chronoamperometry was utilized to evaluate the stability of the bare Ni foam and $NiCo_2S_4$/Ni foam electrodes at 0.60 V versus Ag/AgCl over a duration of 7200 s. As shown in Figure 7b, the CV curve of the bare NF is almost a straight line, which indicates the bare Ni foam exhibits minimal electrocatalytic activity for MOR and the catalytic performance is primarily derived from the $NiCo_2S_4$ active material. The $NiCo_2S_4$/Ni foam electrode's current density declines gradually over time, retaining 90.5% of its initial value after 7200 s. Figure 7c illustrates the CV curves of the $NiCo_2S_4$/Ni foam electrode in a fresh 1 mol dm^{-3} KOH electrolyte with 0.5 mol dm^{-3} methanol before and after the chronoamperometry test for 7200 s. The current density at 0.60 V retains 94.2% of its initial value, with the minor reduction likely attributed to the decreased methanol concentration surrounding the $NiCo_2S_4$ in the process of the test. The above results highlight $NiCo_2S_4$'s commendable electrocatalytic durability and stability for MOR in an alkaline electrolyte.

The impressive electrocatalytic activity and stability of the hierarchical $NiCo_2S_4$ can be attributed to several factors. Firstly, the hierarchical nanostructure of $NiCo_2S_4$ provides a large electrochemical active area and abundant catalytic reaction active sites, favoring electrocatalytic reactions. Secondly, Ni and Co ions have abundant valence states, and the rapid reversible redox reactions between Ni and Co ions in different valence states are beneficial to the methanol oxidation reaction. Lastly, Ni foam can be used as a high-speed path for electrons, facilitating the movement of ions and electrons. The direct growth of $NiCo_2S_4$ samples on Ni foam can reduce contact resistance, which also provides strong adhesion and promotes electron transport.

Additionally, the long-term stability of the $NiCo_2S_4$/Ni foam electrode was probed by performing CV curves of 1000 cycles. Figure 7d exhibits the CV curves acquired at the first, 1000th, and 1001st cycles, and the current density of the $NiCo_2S_4$ sample at 0.60 V is separately 194, 119, and 140 mA mg^{-1}, respectively. It can be seen that the current density retains 61.3% of its original value after 1000 cycles. In addition, in order to eliminate the influence of methanol concentration on the cycling stability of the electrocatalyst, a mixture of KOH and methanol with the same concentration was selected to replace the electrolyte in the 1000th cycle. The CV curve of the 1001st cycle was tested, and it was found that the current density recovered to 72.2% of the initial value. This suggests that the current density reduction is, to some extent, due to methanol depletion during the cycling test. However, a residual decline is observed, which may be attributed to $NiCo_2S_4$ oxidation during the test. As seen in Figure 8, the EDX spectra of the $NiCo_2S_4$ sample, tested before and after 1000 cycles, reveal a significant increase in oxygen content post-cycling. Earlier

reports on $NiCo_2S_4$ indicate suboptimal cycling stability due to the surface oxidation of $NiCo_2S_4$ in an alkaline electrolyte [33,34]. Therefore, the surface oxidation that occurs on the $NiCo_2S_4$ catalyst under an alkaline electrolyte condition appears to be the primary cause of current density degradation during the cycling test.
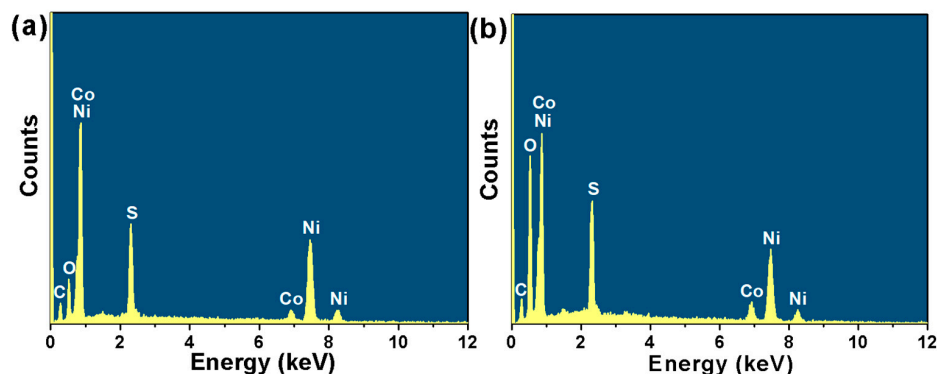
Figure 8. EDX spectra of the $NiCo_2S_4$: (**a**) before the cycling test; (**b**) after the cycling test.

Charge transfer resistance is a key factor affecting the electrocatalytic activity and stability of active materials. The electrical conductivity changes of the electrode materials were studied through the EIS test of $NiCo_2S_4$/Ni foam electrodes in the range of 0.01–100 kHz. Figure 9 shows the Nyquist plots of the $NiCo_2S_4$/Ni foam electrode in an electrolyte of 1 mol dm^{-3} KOH with 0.5 mol dm^{-3} methanol at a scanning rate of 10 mV s^{-1} before and after the 1000 cycling test. The beginning of the semicircle on the real axis in the high-frequency region and the diameter and line of the circle in the low-frequency region correspond to the electrolyte resistance, charge transfer resistance, and diffusion resistance, respectively. It can be seen that Nyquist plots are mainly composed of semicircles in the high-frequency region and oblique lines in the low-frequency region. The electrolyte resistance was 1.29 Ω before 1000 CV cycles and increased to 1.51 Ω after 1000 CV cycles. As can be seen from the magnified view of the high-frequency region in the illustration, the diameter of the semicircle does not change significantly after the 1000 CV cycles, indicating that the charge transfer resistance basically remains unchanged before and after the cycle. In addition, the low-frequency region represents Warburg impedance. It displays that the slopes of the two oblique lines in the low-frequency region are basically the same, indicating that the Warburg impedance of the active material before and after the 1000 cycles is approximately the same. The above results indicate that the $NiCo_2S_4$/Ni foam electrode has good conductivity and stability in the catalytic process.
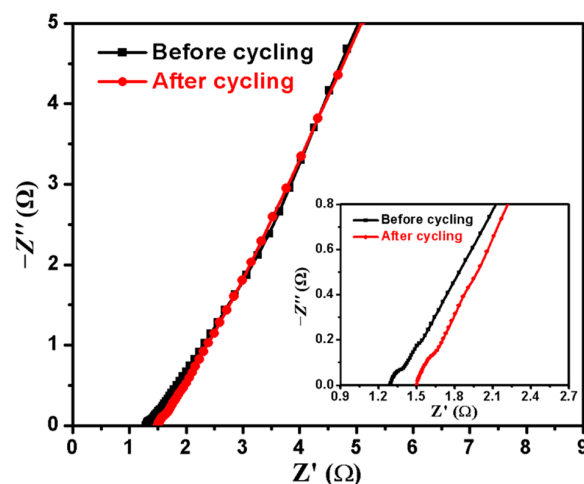
Figure 9. Nyquist plots of the $NiCo_2S_4$/Ni foam electrode before and after the 1000th cycling test (inset shows the magnified view of the high-frequency region).

3. Experimental

3.1. Materials

The materials used were cobalt chloride hexahydrate ($CoCl_2·6H_2O$), nickel chloride hexahydrate ($NiCl_2·6H_2O$), urea ($CO(NH_2)_2$), potassium hydroxide (KOH), hydrochloric acid (HCl), ethanol (C_2H_5OH), methanol (CH_3OH), and distilled water. All chemicals were purchased from Sinopharm Chemical Reagent Co., Ltd. (Beijing, China) and were used as analytical reagents without further purification.

3.2. Synthesis Process of the $NiCo_2S_4$, NiS, and Co_9S_8 Samples

$NiCo_2S_4$ grown on Ni foam had been achieved by a twostep hydrothermal method. The synthesis process involved hydrothermal synthesis and hydrothermal anion exchange. In the first step, Ni^{2+}, Co^{2+}, and $CO(NH_2)_2$ were used as raw materials to obtain the pink precursor loaded on Ni foam by the hydrothermal solvent method. The specific experimental process is as follows: 0.0951 g of $CoCl_2·6H_2O$, 0.0475 g of $NiCl_2·6H_2O$, and 0.3003 g of $CO(NH_2)_2$ were added to 30 mL of distilled water and magnetically stirred for 30 min. Furthermore, the resulting light pink solution was added to a 50-milliliter stainless steel autoclave. A 3 cm × 3 cm piece of nickel foam had been sealed with 1 mol dm^{-3} HCl in order to remove the oxide layer and subsequently rinsed with distilled water and ethanol. The Ni foam was dried and placed vertically into the light pink solution above. The autoclave was placed in an oven and heated at 373 K for 8 h. After the reaction, the Ni foam loaded with pink precursor was taken out and washed several times with distilled water and ethanol before drying for later use.

In the subsequent step, 0.4804 g of $Na_2S·9H_2O$ was dissolved in 30 mL of distilled water and stirred for 10 min to dissolve. The Ni foam loaded with the precursor is placed in the Na_2S solution, which was placed in the stainless steel and heated at 383 K for 4 h. We were following a similar procedure as described earlier to deal with the Ni foam after the reaction. The precursor is converted to $NiCo_2S_4$ by a hydrothermal anion exchange process. The detailed preparation process is shown in Scheme 1. The mass loading of $NiCo_2S_4$ on Ni foam was approximately 0.9 mg cm^{-2}.
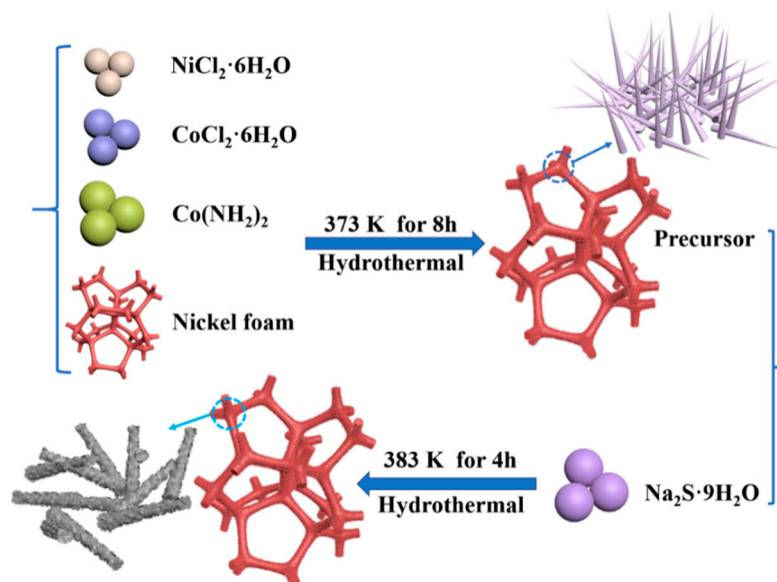
Scheme 1. Schematic diagram for the synthesis of $NiCo_2S_4$ on Ni foam.

For comparison, we also synthesized metal sulfide NiS and Co_9S_8 nanomaterials on Ni foam. The synthesis process is almost exactly the same as that of the $NiCo_2S_4$ nanomaterials mentioned above, except that $CoCl_2·6H_2O$ or $NiCl_2·6H_2O$ is removed from raw materials under other conditions being constant.

3.3. Characterizations

The crystal structure of the sample was characterized by X-ray powder diffraction (XRD, Bruker D8 Advance, Karlsruhe, Germany) using a Cu-Kα radiation source (λ = 0.154060 nm). The morphology of the sample was photographed by a scanning electron microscope (SEM, Hitachi S-8100, Tokyo, Japan), and the working voltage was 5 Kv. Energy dispersive X-ray spectra (EDX) were collected by an attachment to the SEM. The morphology was further studied by a transmission electron microscope (TEM, Hitachi HT-7700, Tokyo, Japan), whose working voltage is 120 Kv. The composition of the sample and the valence distribution of the elements on the surface were tested using X-ray photoelectron spectroscopy (XPS, ESCALab MKII, Thermo Fisher Scientific Inc., Waltham, MA, USA), and the surface charge was treated with an electron neutralizer during XPS analysis. The N_2 adsorption-desorption isotherms were measured at liquid nitrogen temperature (77 K) using a specific surface area analyzer (BET, Micromeritics ASAP 2460, Norcross, GA, USA). The specific surface area was calculated by the Brunauer-Emmett-Teller method.

3.4. Electrochemical Measures

All the electrochemical tests were carried out on the electrochemical analyzer (CHI760E, CHI Ins., Shanghai, China). The tests were measured at room temperature using a three-electrode cell. The foam nickel loaded with active material was cut into 1 cm $\times$ 1 cm pieces, which were directly used as the working electrode, a Pt plate electrode as the counter electrode, and an Ag/AgCl electrode as the reference electrode, respectively. The electrochemical testing methods used in the experiment mainly include cyclic voltammetry (CV), chronoamperometry (CA), and electrochemical impedance spectroscopy (EIS). A 1 mol dm^{-3} KOH solution was selected as the electrolyte for the electrochemical test. CV was performed at a scan rate of 10 mV s^{-1} in the range of 0–0.60 V (vs. Ag/AgCl), and CA lasted for 7200 s at 0.60 V. The EIS test was performed with an amplitude of 5 mV in the frequency range of 0.01 Hz–100 kHz.

4. Conclusions

In conclusion, hierarchical $NiCo_2S_4$ nanomaterials, supported by Ni foam, have been successfully prepared via a simple and economical two-step hydrothermal method. Such a hierarchical structure, constituted by a $NiCo_2S_4$ nanorod core wrapped with a thin nanoribbon shell, has demonstrated its effective facilitation of electrocatalytic reactions. As an electrocatalyst for methanol electrooxidation, the $NiCo_2S_4$ active nanomaterials have shown superior performance, with a current density of 194 mA mg^{-1} at 0.60 V for the $NiCo_2S_4$/Ni foam electrode. In addition, because of the synergistic effect between metal ions and its more abundant redox properties, the Ni-Co binary metal sulfide shows better electrocatalytic activity than the relevant Ni and Co mental sulfide. As a result, these Ni-Co binary metal sulfides may hold certain advantages as non-noble electrocatalysts used in DMFCs. Nonetheless, long-term stability tests have highlighted surface oxidation of the $NiCo_2S_4$/Ni foam electrode in an alkaline electrolyte as a primary factor contributing to current density degradation. Addressing this issue to improve the long-term stability of $NiCo_2S_4$ will be the focus of our future work. This enhancement is anticipated to expand the possibilities for the development and application of non-noble metal electrocatalysts in methanol oxidation reactions.

Data Availability Statement: The data appearing in this paper can be obtained from the first author.

Conflicts of Interest: The authors declare no conflict of interest.

References

1. Wang, Z.B.; Yin, G.P.; Shi, P.F. Effects of ozone treatment of carbon support on Pt-Ru/C catalysts performance for direct methanol fuel cell. *Carbon* **2006**, *44*, 133–140. [CrossRef]
2. Kamarudin, S.K.; Achmad, F.; Daud, W.R.W. Overview on the application of direct methanol fuel cell (DMFC) for portable electronic devices. *Int. J. Hydrogen Energy* **2009**, *34*, 6902–6916. [CrossRef]
3. Gao, M.R.; Gao, Q.; Jiang, J.; Cui, C.H.; Yao, W.T.; Yu, S.H. A methanol-tolerant Pt/CoSe$_2$ nanobelt cathode catalyst for direct methanol fuel cells. *Angew. Chem. Int. Ed.* **2011**, *50*, 4905–4908. [CrossRef] [PubMed]
4. Debe, M.K. Electrocatalyst approaches and challenges for automotive fuel cells. *Nature* **2012**, *486*, 43–51. [PubMed]
5. Xia, Z.; Xu, X.; Zhang, X.; Li, H.; Wang, S.; Sun, G. Anodic engineering towards high performance direct methanol fuel cells with non-precious-metal cathode catalyst. *J. Mater. Chem. A* **2020**, *8*, 1113–1119. [CrossRef]
6. Li, W.; Song, Z.; Deng, X.; Fu, X.Z.; Luo, J.L. Decoration of NiO hollow spheres composed of stacked nanosheets with CeO$_2$ nanoparticles: Enhancement effect of CeO$_2$ for electrocatalytic methanol oxidation. *Electrochim. Acta* **2020**, *337*, 135684. [CrossRef]
7. Xu, X.; Xia, Z.; Zhang, X.; Sun, R.; Sun, X.; Li, H.; Wu, C.; Wang, J.; Wang, S.; Sun, G. Atomically dispersed Fe-N-C derived from dual metal-organic frameworks as efficient oxygen reduction electrocatalysts in direct methanol fuel cells. *Appl. Catal. B Environ.* **2019**, *259*, 118042. [CrossRef]
8. Zhang, X.; Xia, Y.; Gong, X.; Geng, P.; Gao, Z.; Wang, Y. Preparation of sulfonated polysulfone/sulfonated titanium dioxide hybrid membranes for DMFC applications. *J. Appl. Polym. Sci.* **2020**, *137*, 48938. [CrossRef]
9. Tian, H.; Yu, Y.; Wang, Q.; Li, J.; Rao, P.; Li, R.; Du, Y.; Jia, C.; Luo, J.; Deng, P.; et al. Recent advances in two-dimensional Pt based electrocatalysts for methanol oxidation reaction. *Int. J. Hydrogen Energy* **2021**, *46*, 31202–31215. [CrossRef]
10. Huang, H.; Zhu, J.; Li, D.; Shen, C.; Li, M.; Zhang, X.; Jiang, Q.; Zhang, J.; Wu, Y. Pt nanoparticles grown on 3D RuO$_2$-modified graphene architectures for highly efficient methanol oxidation. *J. Mater. Chem. A* **2017**, *5*, 4560–4567. [CrossRef]
11. Xu, H.; Shang, H.; Wang, C.; Jin, L.; Chen, C.; Du, Y. Nanoscale engineering of porous Fe-doped Pd nanosheet assemblies for efficient methanol and ethanol electrocatalyses. *Nanoscale* **2020**, *12*, 2126–2132. [CrossRef]
12. Lou, W.; Ali, A.; Shen, P.K. Recent development of Au arched Pt nanomaterials as promising electrocatalysts for methanol oxidation reaction. *Nano Res.* **2022**, *15*, 18–37.
13. Li, S.; Tian, Z.Q.; Liu, Y.; Jang, Z.; Hasan, S.W.; Chen, X.; Tsiakaras, P.; Shen, P.K. Hierarchically skeletal multi-layered Pt-Ni nanocrystals for highly efficient oxygen reduction and methanol oxidation reactions. *Chin. J. Catal.* **2021**, *42*, 648–657. [CrossRef]
14. Zhang, P.; Bin, D.; Wei, J.S.; Niu, X.Q.; Chen, X.B.; Xia, Y.Y.; Xiong, H.M. Efficient oxygen electrocatalyst for Zn-air batteries: Carbon dots and Co$_9$S$_8$ nanoparticles in a N, S-codoped carbon matrix. *ACS Appl. Mater. Interfaces* **2019**, *11*, 14085–14094. [CrossRef] [PubMed]
15. Yang, Y.; Yao, H.; Yu, Z.; Islam, S.M.; He, H.; Yuan, M.; Yue, Y.; Xu, K.; Hao, W.; Sun, G.; et al. Hierarchical nanoassembly of MoS$_2$/Co$_9$S$_8$/Ni$_3$S$_2$/Ni as a highly efficient electrocatalyst for overall water splitting in a wide pH range. *J. Am. Chem. Soc.* **2019**, *141*, 10417–10430. [CrossRef] [PubMed]
16. Huo, H.; Zhao, Y.; Xu, C. 3D Ni$_3$S$_2$ nanosheet arrays supported on Ni foam for high-performance supercapacitor and non-enzymatic glucose detection. *J. Mater. Chem. A* **2014**, *2*, 15111–15117. [CrossRef]
17. Zhang, Y.; Chao, S.; Wang, X.; Han, H.; Bai, Z.; Yang, L. Hierarchical Co$_9$S$_8$ hollow microspheres as multifunctional electrocatalysts for oxygen reduction, oxygen evolution and hydrogen evolution reactions. *Electrochim. Acta* **2017**, *246*, 380–390. [CrossRef]
18. Qian, L.; Chen, W.; Huang, R.; Xiao, D. Direct growth of NiCo$_2$S$_x$ nanostructures on stainless steel with enhanced electrocatalytic activity for methanol oxidation. *RSC Adv.* **2015**, *5*, 4092–4098. [CrossRef]
19. Jin, D.; Li, Z.; Wang, Z.H. Hierarchical NiCo$_2$O$_4$ and NiCo$_2$S$_4$ nanomaterials as electrocatalysts for methanol oxidation reaction. *Int. J. Hydrogen Energy* **2021**, *46*, 32069–32080. [CrossRef]
20. Zhu, Y.; Wu, Z.; Jing, M.; Yang, X.; Song, W.; Ji, X. Mesoporous NiCo$_2$S$_4$ nanoparticles as high-performance electrode materials for supercapacitors. *J. Power Sources* **2015**, *273*, 584–590. [CrossRef]
21. Feng, X.; Jiao, Q.; Cui, H.; Yin, M.; Li, Q.; Zhao, Y.; Li, H.; Zhou, W.; Feng, C. One-pot synthesis of NiCo$_2$S$_4$ hollow spheres via sequential ion exchange as an enhanced oxygen bifunctional electrocatalyst in alkaline solution. *ACS Appl. Mater. Interfaces* **2018**, *10*, 29521–29531. [CrossRef] [PubMed]
22. Liang, Y.X.; Gong, Q.J.; Sun, X.L.; Xu, N.N.; Gong, P.N.; Qiao, J.L. Rational fabrication of thin-layered NiCo$_2$S$_4$ loaded graphene as bifunctional non-oxide catalyst for rechargeable zinc-air batteries. *Electrochim. Acta* **2020**, *342*, 136108. [CrossRef]
23. Dong, M.X.; Wang, Z.X.; Yan, G.C.; Wang, J.X.; Guo, H.J.; Li, X.H. Confine growth of NiCo$_2$S$_4$ nanoneedles in graphene framework toward high-performance asymmetric capacitor. *J. Alloys Compd.* **2020**, *822*, 153645. [CrossRef]
24. Gao, Y.; Wu, B.; Hei, J.; Gao, D.; Xu, X.; Wei, Z.; Wu, H. Self-assembled synthesis of waxberry-like open hollow NiCo$_2$S$_4$ with enhanced capacitance for high-performance hybrid asymmetric supercapacitors. *Electrochim. Acta* **2020**, *347*, 136314. [CrossRef]

25. Jin, D.; Li, Z.; Ma, T.T.; Wang, Z.H. Three-dimensional flower-like Mn-Ni-Co-O microstructure as a high-performance electrocatalyst for methanol oxidation reaction. *New J. Chem.* **2022**, *46*, 7657–7662. [CrossRef]

26. Li, X.; Liu, J.; Zhang, J.; Wu, S.; Zhang, D.; Shui, J. Interface engineering of $NiCo_2O_4$/BCN nanotube for performance enhancement of lithium-oxygen battery. *Chem. Eng. J.* **2021**, *411*, 128403. [CrossRef]

27. Feng, X.; Jiao, Q.; Chen, W.; Dang, Y.; Dai, Z.; Suib, S.L.; Zhang, J.; Zhao, Y.; Li, H.; Feng, C. Cactus-like $NiCo_2S_4$@NiFe LDH hollow spheres as an effective oxygen bifunctional electrocatalyst in alkaline solution. *Appl. Catal. B Environ.* **2021**, *286*, 119869. [CrossRef]

28. Singh, B.S.; Ibomcha, I.T.; Dai, J.Y.; Kshetri, T.; Kim, N.H.; Lee, J.H. Flexible transparent supercapacitor with core-shell Cu@Ni@NiCoS nanofibers network electrode. *Chem. Eng. J.* **2020**, *395*, 125019.

29. Ao, D.; Shi, Y.; Li, S.; Chang, Y.; Xu, A.; Jia, J.; Jia, M. 3D Co-Ni-C network from milk as competitive bifunctional catalysts for methanol and urea electrochemical oxidation. *Catalysts* **2021**, *11*, 844. [CrossRef]

30. Yuan, F.; Wei, J.; Qin, G.; Ni, Y. Carbon cloth supported hierarchical core-shell $NiCo_2S_4$@CoNi-LDH nanoarrays as catalysts for efficient oxygen evolution reaction in alkaline solution. *J. Alloys Compd.* **2020**, *830*, 154658. [CrossRef]

31. Chen, H.; Jiang, J.; Zhang, L.; Wan, H.; Qi, T.; Xia, D. Highly conductive $NiCo_2S_4$ urchin-like nanostructures for high-rate pseudocapacitors. *Nanoscale* **2013**, *5*, 8879–8883. [CrossRef] [PubMed]

32. Yi, T.F.; Li, Y.M.; Wu, J.Z.; Xie, Y.; Luo, S. Hierarchical mesoporous flower-like $ZnCo_2O_4$@NiO nanoflakes grown on nickel foam as high-performance electrodes for supercapacitors. *Electrochim. Acta* **2018**, *284*, 128–141. [CrossRef]

33. Huang, Y.; Shi, T.; Jiang, S.; Cheng, S.; Tao, X.; Zhong, Y.; Liao, G.; Tang, Z. Enhanced cycling stability of $NiCo_2S_4$@NiO core-shell nanowire arrays for all-solid-state asymmetric supercapacitors. *Sci. Rep.* **2016**, *6*, 38620. [CrossRef]

34. He, G.; Qiao, M.; Li, W.; Lu, Y.; Zhao, T.; Zou, R.; Li, B.; Darr, J.A.; Hu, J.; Titirici, M.M.; et al. S, N-Co-doped graphene-nickel cobalt sulfide aerogel: Improved energy storage and electrocatalytic performance. *Adv. Sci.* **2017**, *4*, 1600214. [CrossRef] [PubMed]